

Computational confocal tomography for simultaneous reconstruction of objects, occlusions, and aberrations

Keith Dillon* and Yeshaiahu Fainman

Department of Electrical and Computer Engineering, University of California, San Diego,
9500 Gilman Drive, La Jolla, California 92093-0407, USA

*Corresponding author: kdillon@ucsd.edu

Received 26 August 2009; revised 14 February 2010; accepted 9 April 2010;
posted 12 April 2010 (Doc. ID 116180); published 27 April 2010

We introduce and experimentally validate a computational imaging technique that employs confocal scanning and coherent detection in the Fourier domain. We show how this method may be used to tomographically reconstruct attenuation, aberration, and even occlusion. We also show how these image parameters may be combined with the conventional confocal image reconstruction of the object reflectivity. We demonstrate the method experimentally by imaging a sample consisting of an occlusion above a mirror of varying reflectivity. © 2010 Optical Society of America

OCIS codes: 110.1758, 110.6955.

1. Introduction

Optical imaging techniques may be separated into two categories based on whether image formation is performed by optical components or computationally with the help of a computer. Confocal microscopy is the simplest example that straddles these two categories by using a computer to assemble the three-dimensional image, whereas each pixel (or voxel) is formed purely optically by scanning the source relative to the sample [1].

Computational approaches for optical image formation based on tomographic reconstruction were developed, along with tomography techniques, during the past decades. The confocal scanning microscopy method is sometimes referred to as tomography, as it, indeed, forms slices of the image. In this manuscript, however, we use the term “tomography” to refer to more computationally intense and novel reconstruction methods that we called “computational confocal tomography.” The key to computed tomography is the collection of projections of the data

over a range of angles, to produce a Radon transform of the image [2]. The image of the data is then reconstructed using an inverse Radon transform technique, such as filtered backprojection. The vast majority of development of this method originated in the field of medical imaging, utilizing x-ray fields [3]. Various optical systems that use collimated light beams have been developed to produce an optical analog of the x-ray projection approach, employing the approximation that the light rays follow straight lines paths. However, the large amount of scattering encountered at optical frequencies, as opposed to x rays, caused difficulty with this assumption. Techniques to more accurately satisfy the small-angle assumption for validity of the Born or Rytov approximations [4], as well as diffuse optical tomography [5] methods (at the large scattering-angle extreme) have been developed and demonstrated.

Of course, scattering properties of the object vary, depending on the specific application. For example, for the microscopic imaging of cells, they pose an opposite problem, as the refractive index variations between many cellular structures are very small [6]. Fortunately, advances in interferometry have enabled the measurement of very small phase

variations [7], and this, in turn, enables potential imaging of these structures via their refractive index. Furthermore, Wedberg *et al.* [8] investigated some basic examples that show negligible improvement provided by using the Born approximation over the straight-ray approximation for phase objects, which lends further credence to this straight-ray approximation.

Of course, imaging the sample attenuation coefficient is itself possible by measurement of intensity instead of phase. Katawa *et al.* [9] produced images of spirogyra in a system that essentially achieves rotation of the sample within a collimated beam. This fairly direct application of computed tomography to optics is the most common approach. Zysk *et al.* [10] demonstrated image formation of a purely refractive sample, where the data was collected in this fashion. Their “projected index computed tomography” method uses standard backprojection techniques to reconstruct the image under the straight-ray assumption. Renaud *et al.* [11] demonstrated a conceptually similar technique that is called “confocal axial tomography,” employing microfluidics to rotate cells within the light beam. Sharpe *et al.* [12] also employed rotation of a large size object such that the depth of focus of the illumination/detection beam had to be taken into consideration.

Less commonly, systems employ a focused beam. Kikuchi *et al.* [13] considered so-called multiple axis imaging systems, where multiple microscopes with foci at different angles were intersected, effectively treating the source near the focus as a very small collimated beam. Vishnyakov *et al.* [14] constructed a system in which the sample was placed on a mirror in an interferometer, while the focal point was scanned along the mirror by displacing the point source in the conjugate plane, in order to reconstruct the refractive index. This is done by using the angular spread of the rays themselves, more akin to cone-beam tomography. This system is also interesting in that, unlike those previously discussed, Vishnyakov’s system operates in a reflective mode. Lue *et al.* [15] described a similar concept that employs a focused line beam scanned through a sample flowing in a microfluidic channel, with a cylindrical objective lens. Marks *et al.* [16] derive and simulate an approach to the estimate group refractive index, wherein they derive a solution for a tomographic measurement with a high numerical aperture.

These systems also demonstrate the ability to produce tomographic images of microscopic structures, such as cellular structures, though the straight-ray approximation, and for that matter ray optics itself, becomes less applicable in this microscopic regime. For example, Vishnyakov *et al.* [14] produced images of a lymphocyte. Renaud *et al.* [11] produced images of SW13 cells. The approaches used apply, or could be adapted to apply, to the attenuation and refractive index of the volume illuminated by the light. But the physical effects at the focus itself, for the systems that use a focused beam, are not exploited.

As is the case in confocal microscopy, the ideal mode for such a system is often reflective, whereby depth sections of thick samples may be collected. In confocal microscopy, the focus (of both source and detection objective) is reimaged onto a pinhole that rejects light scattered from elsewhere in the sample. This forms the basis for a variety of imaging techniques. In this paper, we further consider the problem of performing computational reconstruction of the sample at the same time as the imaging of the object at focus. Hence we describe this technique as “computational confocal,” as we are computationally reproducing the signal at the pinhole. However instead of rejecting the scattered light outside the pinhole, we assume that this scatter will be negligible (except from the focus itself) and instead use the entire aperture of light, to also reconstruct the sample volume between the focus and the objective without need for depth scanning. We view the method described here to be a superset of conventional confocal imaging for low scattering situations, which we believe provides a novel and useful perspective.

This is also the first demonstration, to our knowledge, of the combination of scanned object imaging with computed tomography reconstruction. We demonstrate the ability to collect data “around” an occlusion, in order to image the object behind it, which we believe is a potentially very useful advance in microscopy.

In this manuscript we show how to use a series of translational steps during the data collection process where we collect a high-numerical aperture signal, rather than collect a series of projections over successive angles with a collimated beam. In effect, rather than serially filling out a desired angular range with a fixed field of view, we fill out a desired field of view with a fixed angular range. The total collected angular bandwidth range within each measurement is determined by the numerical aperture of the microscope objective, suggesting use of modern high-numerical aperture objectives to cover large angular bandwidth.

A diagram of the computational imaging system that we investigate here is provided in Fig. 1(a), shown in comparison with a similar confocal three-dimensional scanning system. It is evident that our system requires only limited modifications be made to the conventional confocal imaging system.

Both systems use a collimated laser source that is focused and is being scanned within the volume of the object, but in contrast to conventional confocal microscopy that relies on three-dimensional volume scanning, our system performs a single scan in the transverse direction. In our approach the three-dimensional information is reconstructed from the collected data. Furthermore, we detect the entire complex signal of the Fourier transform of the reflected field, rather than reimaging the object on a pinhole and only detecting the intensity of a single point, as is typically performed in confocal imaging (this is equivalent to detecting the “DC” spatial fre-

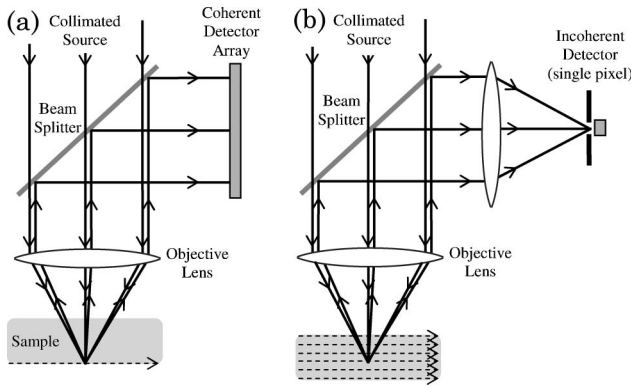


Fig. 1. (a) Computational imaging system versus (b) conventional scanning confocal system. The dashed lines on the sample represent the scanning paths of the focal point as the sample is moved on a translation stage.

quency of the object). In effect, while the conventional confocal system samples a single pixel of the sample volume at each point in the scan, the computational system collects a range of data over the sample volume at each step. In Section 2, we will start from the analysis of our approach by describing how attenuation and refractive index variation may be combined with conventional confocal measurements at the objective focus in a complex attenuation parameter, which can be imaged. Section 2 will also show how the complex confocal image data may be viewed as a rearrangement of projection data to which tomographic reconstruction can be applied. In Section 3 we describe the experimental system and apply the new imaging technique to the experimentally measured results for a specially made sample to demonstrate the simultaneous imaging of an occlusion and an object with varying reflectivity beyond it. The conclusions and discussions will be described in Section 4.

2. Analysis of the Computational Confocal Tomography System

To analyze the confocal tomography system introduced in Fig. 1(a), first we describe how attenuation, phase aberrations, and even the scattering or reflectivity at the focal point may all be combined into a complex attenuation parameter that can be imaged as discussed and quantified below.

A. Complex Attenuation Parameter

We simplify the computational system of Fig. 1(a) further by projecting the pixel locations of the coherent detector array to the entrance pupil (i.e., aperture) of the microscope objective [see Fig. 2]. We also neglect the transmission (i.e., illumination) path and assume that we start from a point source located at the focal point of the microscope objective.

For an isotropic scalar spherical wave radiated from the focus at distance d from the observation plane, the spatial component of the optical field signal at any observation point \mathbf{r} would be

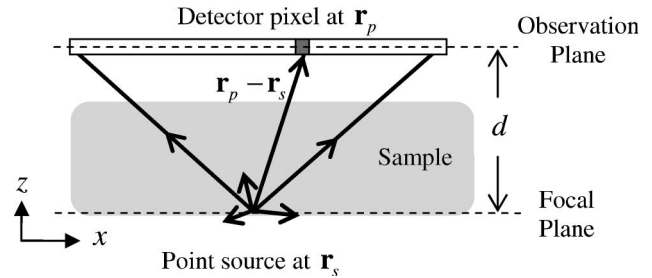


Fig. 2. Geometry of locations of a virtual detector pixel and its physical relationship to the point source, which is assumed to be fixed relative to the detector pixels.

$$u(\mathbf{r}_s, \mathbf{r}) = A \frac{1}{|\mathbf{r} - \mathbf{r}_s|} \exp\{j[k|\mathbf{r} - \mathbf{r}_s|]\}, \quad (1)$$

where A is the value of the amplitude associated with the strength of the particular scattering point (e.g., due to the transmitted amplitude and scattering cross section), \mathbf{r}_s is the point-source location, k is $2\pi/\lambda$ for a monochromatic source with wavelength λ in vacuum, and j is $\sqrt{-1}$. So A is the value we desire in normal confocal imaging.

Generally, the sample volume between the focus and the detector will induce a phase delay and amplitude attenuation (i.e., phase and amplitude modulation) at the detector pixel located at $\mathbf{r} = \mathbf{r}_p$ (see Fig. 2), yielding

$$u(\mathbf{r}_s, \mathbf{r}_p) = a(\mathbf{r}_s, \mathbf{r}_p) A \frac{1}{|\mathbf{r}_p - \mathbf{r}_s|} \exp\{j[k|\mathbf{r}_p - \mathbf{r}_s| + \Delta\phi(\mathbf{r}_s, \mathbf{r}_p)]\}, \quad (2)$$

where $a(\mathbf{r}_s, \mathbf{r}_p)$ is the amplitude attenuation and $\Delta\phi(\mathbf{r}_s, \mathbf{r}_p)$ is the phase delay.

Next we combine all the terms into a complex attenuation coefficient such that Eq. (2) may be rewritten as

$$u(\mathbf{r}_s, \mathbf{r}_p) = \exp\{-\mu(\mathbf{r}_s, \mathbf{r}_p)\}, \quad (3)$$

$$\mu(\mathbf{r}_s, \mathbf{r}_p) = -j[k|\mathbf{r}_p - \mathbf{r}_s| + \Delta\phi(\mathbf{r}_s, \mathbf{r}_p)] - \ln a(\mathbf{r}_s, \mathbf{r}_p) - \ln A + \ln |\mathbf{r}_p - \mathbf{r}_s|. \quad (4)$$

We further break down this complex attenuation function into the sample-independent terms μ_0 and sample-induced terms μ_t , defined by

$$\mu(\mathbf{r}_s, \mathbf{r}_p) = \mu_0(\mathbf{r}_s, \mathbf{r}_p) + \mu_t(\mathbf{r}_s, \mathbf{r}_p), \quad (5)$$

$$\mu_0(\mathbf{r}_s, \mathbf{r}_p) = -jk|\mathbf{r}_p - \mathbf{r}_s| + \ln |\mathbf{r}_p - \mathbf{r}_s|, \quad (6)$$

$$\mu_t(\mathbf{r}_s, \mathbf{r}_p) = -j\Delta\phi(\mathbf{r}_s, \mathbf{r}_p) - \ln a(\mathbf{r}_s, \mathbf{r}_p) - \ln A. \quad (7)$$

The subscript t refers to the fact that this term contains the tomographic information of the sample.

Furthermore, we can describe the phase delay as the result of the refractive index variation integrated along the optical path followed by the light “ray” between \mathbf{r}_p and \mathbf{r}_s :

$$\Delta\phi(\mathbf{r}_s, \mathbf{r}_p) = \int_{\mathbf{r}_s}^{\mathbf{r}_p} k\Delta n(\mathbf{r})ds, \quad (8)$$

where $\Delta n(\mathbf{r})$ is $n(\mathbf{r}) - n_0$, $n(\mathbf{r})$ is the varying index of the sample, and n_0 is the medium index for which the optics is corrected (e.g., air, oil, glass). The integral $\int ds$ refers to the path integral between the points at the integration limits; the specifics of the followed paths will be described below. The attenuation resulting from the integrated attenuation coefficient along the same path is

$$\alpha(\mathbf{r}_s, \mathbf{r}_p) = \exp\left\{-\int_{\mathbf{r}_s}^{\mathbf{r}_p} \alpha(\mathbf{r})ds\right\}. \quad (9)$$

So, the complex attenuation function given in Eq. (7) can be rewritten as

$$\mu_t(\mathbf{r}_s, \mathbf{r}_p) = -j \int_{\mathbf{r}_s}^{\mathbf{r}_p} k\Delta n(\mathbf{r})ds + \int_{\mathbf{r}_s}^{\mathbf{r}_p} \alpha(\mathbf{r})ds - \ln A. \quad (10)$$

Moreover, if we form the impulse function $\delta(\mathbf{r})$ localized at the point source and employ the integral expression

$$\int_{\mathbf{r}_s}^{\mathbf{r}_p} \delta(\mathbf{r} - \mathbf{r}_s)ds = 1, \quad (11)$$

we can define the point-source amplitude A in an integral form as well:

$$\ln A = (\ln A) \int_{\mathbf{r}_s}^{\mathbf{r}_p} \delta(\mathbf{r} - \mathbf{r}_s)ds. \quad (12)$$

We use Eq. (12) in Eq. (10) and combine all the terms into a single integral:

$$\mu_t(\mathbf{r}_s, \mathbf{r}_p) = \int_{\mathbf{r}_s}^{\mathbf{r}_p} \eta_A(\mathbf{r}, \mathbf{r}_s)ds, \quad (13)$$

$$\eta_A(\mathbf{r}, \mathbf{r}_s) = -jk\Delta n(\mathbf{r}) + \alpha(\mathbf{r}) - \delta(\mathbf{r} - \mathbf{r}_s) \ln A. \quad (14)$$

The complex attenuation coefficient describes the attenuation resulting from the sample as an integral

over the path between the point source and the detector pixel.

Our final result combines Eqs. (3), (5), and (13), yielding the observed complex amplitude of the optical field given by

$$u(\mathbf{r}_s, \mathbf{r}_p) = u_0(\mathbf{r}_s, \mathbf{r}_p) \exp\left\{-\int_{\mathbf{r}_s}^{\mathbf{r}_p} \eta_A(\mathbf{r}, \mathbf{r}_s)ds\right\}, \quad (15)$$

where $u_0(\mathbf{r}_s, \mathbf{r}_p)$ is the sample-independent signal from a unit-amplitude source, $\exp\{-\mu_0(\mathbf{r}_s, \mathbf{r}_p)\}$. This is the deterministic component of the signal, which may be partially or completely eliminated by the microscope objective itself (particularly the spherical phase component). Alternatively, it may be detected and computed during the calibration process of the system.

Now we reconsider the difference between the amplitude A , and the attenuation in the sample, $\alpha(\mathbf{r}_s, \mathbf{r}_p)$. We note that $\eta_A(\mathbf{r}, \mathbf{r}_s)$ is a function of \mathbf{r}_s purely due to the term $\delta(\mathbf{r} - \mathbf{r}_s) \ln A$, describing the source location. If we are scanning the sample, then the value of A , which we recall incorporates the source amplitude as well as the reflection or scattering coefficient at the focal point, corresponds to a particular point in the scan. First we assume that the focal point locations are known for every point in the scan (for example, along an object plane). And second we assume we scan in such a way that a point at focus is not illuminated when the system scans to a different focus. Then we may combine the source amplitudes into a complex attenuation function

$$\eta(\mathbf{r}) = -jk\Delta n(\mathbf{r}) + \alpha(\mathbf{r}) - \sum_{m=0}^M \delta(\mathbf{r} - \mathbf{r}_s(m)) \ln A(m), \quad (16)$$

where $\mathbf{r}_s(m)$ and $A(m)$ are the focal point location and the corresponding amplitude for the m th step in the scan (see Fig. 3). We can treat the complex attenuation function plus the object-plane information as independent of the focal point under the condition that none of the rays captured by the detector cross through multiple focal points. Then projections of $\eta_A(\mathbf{r}, \mathbf{r}_s)$ and $\eta(\mathbf{r}, \mathbf{r}_s)$ will be consistent. For transverse scanning, this requirement would hold, whereas for axial scanning it would not. Therefore, in the case of transverse scanning (the technique to be employed in subsequent sections) we may treat the point-source amplitude as an attenuation and assume that the complex attenuation (with the amplitude included) is independent of the focal point. This will be useful when we can reconstruct the complex attenuation and get the amplitude values as part of that result.

B. Scanning Tomography

Next we describe the method for processing the computational confocal scanning data to reconstruct and

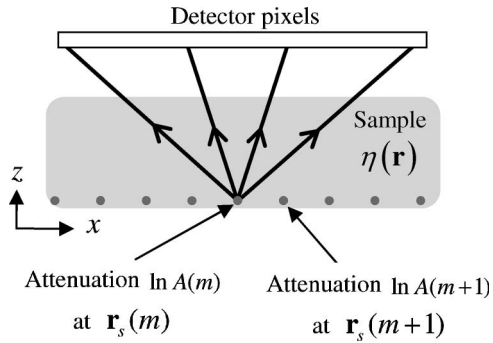


Fig. 3. Definition of the sample as a complex attenuation function $\eta(\mathbf{r})$, which includes the point-source amplitudes in the focal plane of the microscope objective.

view tomographic projection data. For simplicity, we assume a one-dimensional detector array and a one-dimensional scan procedure. We also assume that during the scanning process, the confocal source and detector relative to the sample are moved (we assume the sample is stationary in our analysis, and the optics is translated) by a fixed distance increment equal to the separation between pixels in the detector array, Δx . The vector describing this step is defined by $\Delta \mathbf{x} = (\Delta x, 0)$. Thus at the m th step in the scan, the focal point is at a location

$$\mathbf{r}_s(m) = \mathbf{r}_s^{(0)} + m\Delta \mathbf{x}, \quad (17)$$

where $\mathbf{r}_s^{(0)}$ is the location of the initial focal point. Also at the m th step in the scan, the n th pixel in the detector array has a coordinate at location

$$\mathbf{r}_p(m, n) = \mathbf{r}_p^{(0)} + m\Delta \mathbf{x} + n\Delta \mathbf{x}, \quad (18)$$

and $\mathbf{r}_p^{(0)}$ is the coordinate of the location of the initial pixel at the initial step.

If we consider the complex data collected at each pixel for each scan step, we can enumerate them as $u(\mathbf{r}_s(m), \mathbf{r}_p(m, n))$, or simply $u_{m,n}$ [see Fig. 4 and the matrix representation shown in Fig. 5(a)]. Assuming that the ray paths are all straight lines, and the signal is only affected by a phase delay and attenuation, we can view the data of Fig. 5(a) as a version of the slant stack of tomographic projection data of the sample. Since the rays are assumed to follow straight lines, the focal point has a fixed location relative to the detectors in the array; hence, the angle between the focal point and a given detector pixel will be constant over the scan. For example, if we observe the rays corresponding to the column $[n = 2$ in Fig. 5(a)], they collectively form a projection of the sample at a fixed direction angle, as shown in Fig. 5(b).

By combining Eqs. (17) and (18) with Eq. (15), we obtain

$$u_{m,n} = u_{0;m,n} \exp \left\{ - \int_{\mathbf{r}_s^{(0)} + m\Delta \mathbf{x}}^{\mathbf{r}_p^{(0)} + m\Delta \mathbf{x} + n\Delta \mathbf{x}} \eta(\mathbf{r}) d\mathbf{s} \right\}. \quad (19)$$

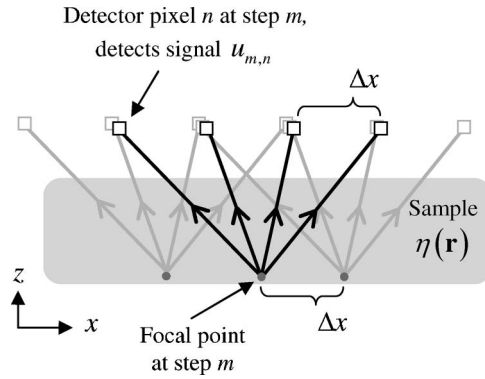


Fig. 4. Schematic diagram describing the detector pixels and the focal point locations at three different steps in a one-dimensional confocal scan of a two-dimensional sample. This example shows four pixels of the photodetector array and three scanning points of the object.

Next we define $p_0(x)$, the projection of $\eta(\mathbf{r})$:

$$p_0(x) = \int_{-\infty}^{\infty} \eta(x, z) dz. \quad (20)$$

Note that, since the detector pixels are always in the same plane, the projections we form at different angles are technically not rotated, but sheared. Figure 6 shows how a sheared version of the sample provides a zero-angle projection. The sheared projection would then be

$$p_\theta(x) = \int_{-\infty}^{\infty} \eta(x - z \tan \theta, z) dz. \quad (21)$$

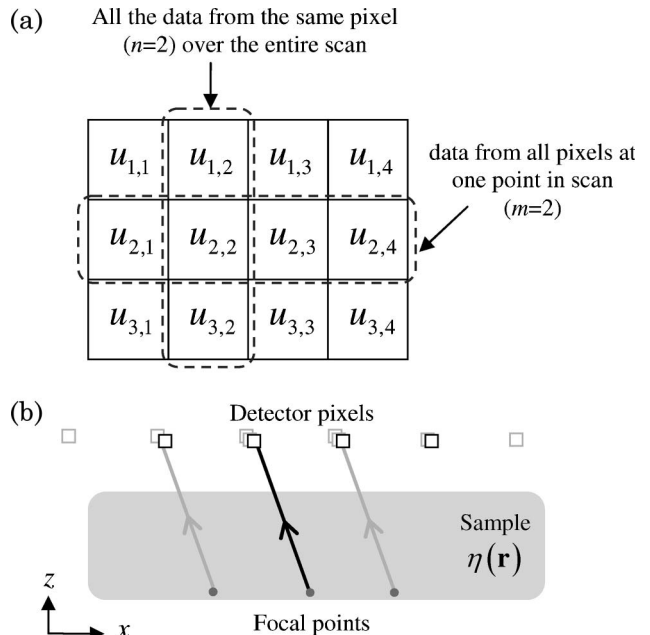


Fig. 5. (a) Matrix representation of the complex data from all pixels over all steps in the scanning process for the example of Fig. 4 for a four-pixel, three-step scan. (b) Rays corresponding to the $(n = 2)$ column of the slant-stack data.

Assuming that the sample is transparent outside the region bounded in z by the focal point and detector (since we are not trying to image those outer regions and they are not illuminated), we may combine Eq. (19) with Eq. (21) to get

$$u_{m,n} = (u_0)_{m,n} \exp\{-p_{\theta(n)}(m\Delta x)\}, \quad (22)$$

where

$$\theta(n) = \tan^{-1}\left(\frac{z_p^{(0)} - z_s^{(0)}}{x_p^{(0)} - x_s^{(0)} + n\Delta x}\right), \quad \mathbf{r}_s^{(0)} = (x_s^{(0)}, z_s^{(0)}),$$

$$\mathbf{r}_p^{(0)} = (x_p^{(0)}, z_p^{(0)}). \quad (23)$$

The complex attenuation is a sampled version of the projection of the complex attenuation coefficient. Furthermore, we see that by collecting data over a range of n and m , we get a range of projection angles over a volume of the sample, forming a subset of the Radon transform of the attenuation coefficient $\eta(\mathbf{r})$. More details are provided in Appendix A, which also addresses the three-dimensional case.

3. Experimental Validation of Computational Confocal Tomography

A. System Implementation

In the experimental validation of the technique, we consider a slightly modified configuration where a sample is located on a planar mirror surface (see Fig. 7). The “source amplitude” is determined by the laser amplitude and the reflectivity of the mirror. Each ray is attenuated by the sample projection in the forward path during illumination, the reflectivity of the mirror, and attenuated by the sample projection in the backscattered path (see Fig. 7)]. We further incorporated large refractive index changes at the air-sample interface, by refracting the rays via Snell’s law (see Fig. 7). Also, the air-sample interface may not be a concern if the sample is only expected to vary beneath the coverslip, as long as the projection angles are properly adjusted. This only requires knowledge of the sample thickness, which we estimate using the quadratic term in the measured phase error.

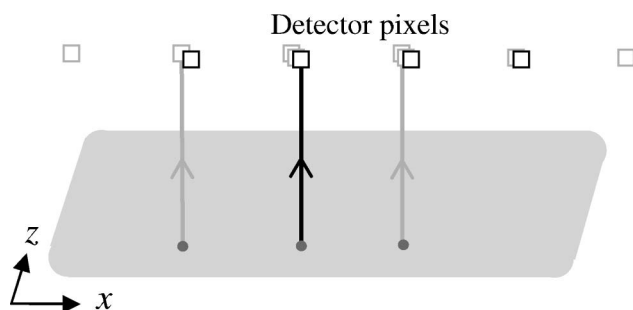


Fig. 6. Rays corresponding to the ($n = 2$) column of the slant-stack data with sheared coordinates to obtain vertical projection.

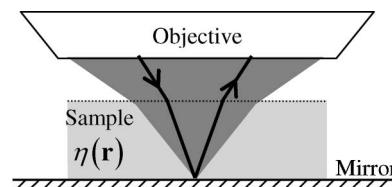


Fig. 7. Description of a sample-on-mirror system.

To collect the complex amplitude data, we employed a standard Michelson interferometer, shown schematically in Fig. 8. A replica of the source and the signal returning from the sample interfere, and the interference pattern is detected by a digital camera. The detected phase must be unwrapped; for this experiment, the MATLAB built-in *unwrap* function performed the task sufficiently.

In the experiments we use a Nikon plano apochromat objective with a numerical aperture of 0.75, which provides about 97° of angular bandwidth spread in the air (i.e., above the coverslip). The source was a 10 mW He-Ne laser at 632.8 nm, and a SBIG ST-402 camera was used to record the interference pattern magnified using a standard telecentric imaging system to a pixel spacing of $3.0 \mu\text{m}$. The sample was placed on the mirror at the working distance of the objective, and the mirror was mounted on a translation stage, which was moved transversely to the optical beam. The camera pixel spacing effectively achieves $3.0 \mu\text{m}$ sampling at the entrance aperture of the objective. The sample was moved by a translation stage in steps of $3.0 \mu\text{m}$ between image captures, using a Physik Instrumente C-844 controller and M224 motors. We performed a one-dimensional scan, and, hence, the slant stack and final image are two dimensional. As described earlier, each complex data set recorded at the detec-

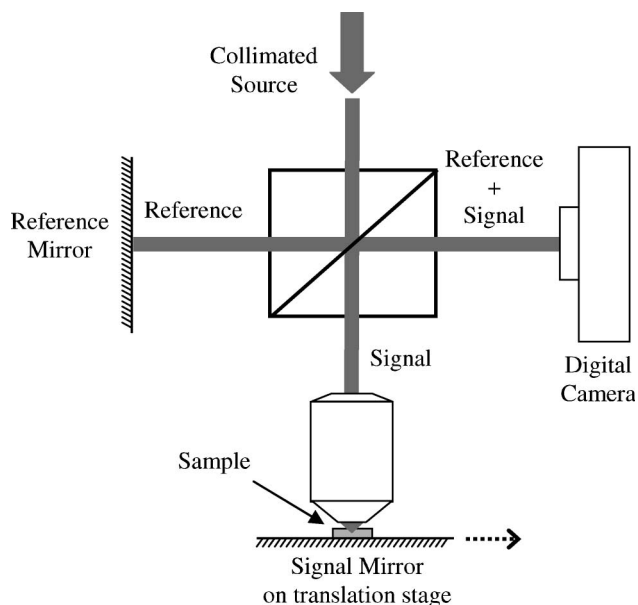


Fig. 8. Schematic diagram of a spatial heterodyne system for detection of the complex amplitude of the signal from the object.

tor at a point in the scan provides a new row for the slant stack (see Fig. 5).

B. Reconstruction of the Sample Image

To demonstrate the capability of our method to reconstruct the image in the presence of occlusion and varying reflectivity and to validate the performance of the method experimentally, we prepared a special sample. The sample consists of nonreflective stripes printed on the mirror. We also placed a coverslip over the mirror and placed an opaque fiber onto the coverslip, parallel to the stripes, as shown in Fig. 9.

The sample (see Fig. 9) was scanned in one dimension along the direction perpendicular to the fiber and the opaque stripes (x direction in Fig. 9); thus, the reconstructed image would provide a two-dimensional cross section of the sample similar to that shown in Fig. 9(b). The slant-stack data collected for this sample are shown in Fig. 10, both with and without the correction of the deterministic term $u_0(\mathbf{r}_s, \mathbf{r}_p)$.

The camera image was averaged over the perpendicular direction (y direction) to produce the row of slant-stack data. Note that the final image will be in the $x-z$ plane. As the image shows, there were approximately 750 pixels across the camera, and the image was captured for 400 scanning steps. The dark horizontal bands of the slant stack correspond to the images where the focus was on the dark stripes on the mirror; hence, there was no return signal at all. The diagonal bands correspond to the partial occlusion caused by the fiber, as it moves across the beam. There are two such stripes because it occluded both the converging signal before reflecting on the mirror, and the diverging signal after reflection.

The inverse Radon transform of this data was computed using filtered backprojection (using the

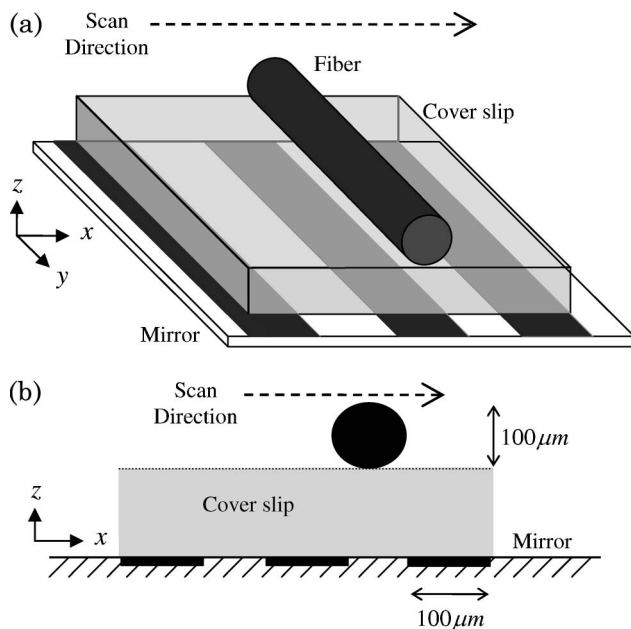


Fig. 9. Description of the measured sample: (a) three-dimensional view and (b) cross-sectional view.

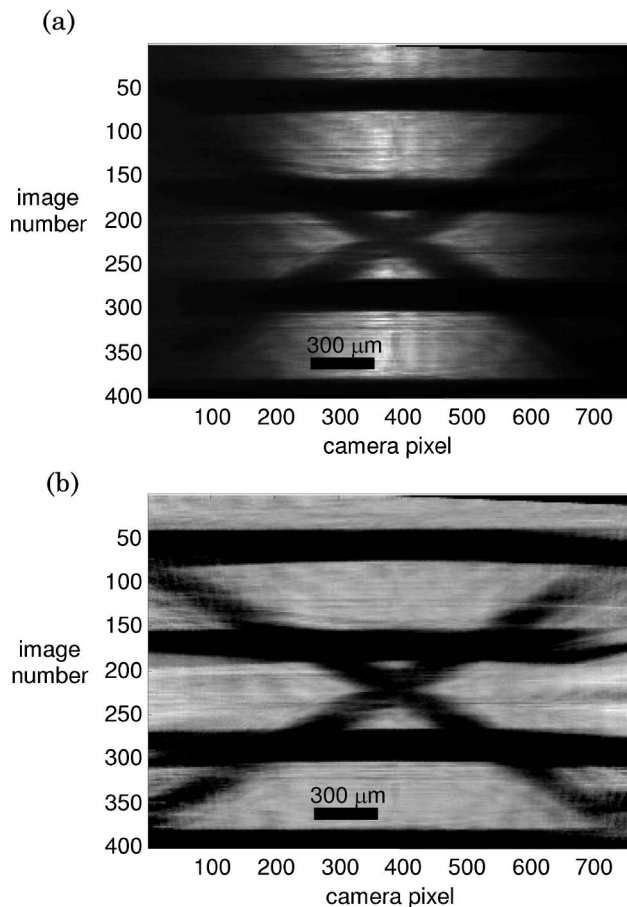


Fig. 10. Amplitude of slant stack for the sample of Fig. 9: (a) raw and (b) corrected for deterministic variation.

piecewise-linear rays described earlier) to produce the image shown in Fig. 11. As the attenuation is defined to be positive everywhere, we were able to reduce artifacts by clamping the data values at zero. Furthermore, the stripes were much darker than the fiber, so saturation of the pixel values was performed to allow the weaker fiber image to be more visible. The experimental results in Fig. 11 show that the image of the stripes and the fiber can be distinguished.

4. Discussion

We show how the data from the aperture of a scanning confocal system can be used to perform a tomographic reconstruction of the sample attenuation and refractive index, as well as the reflectivity at the focal point. We demonstrated this method experimentally in two dimensions, using a sample consisting of a varying reflectivity mirror with an occluding object above it. The approach assumes minimal scattering and that ray paths follow straight lines within the sample.

The axial resolution within the straight-ray approximation for the tomographic reconstruction corresponds to approximately $2.6 \mu\text{m}$, assuming that it is based on collected spatial bandwidth representing a point. Of course, this is an incomplete description of the imaging performance, as this bandwidth is only

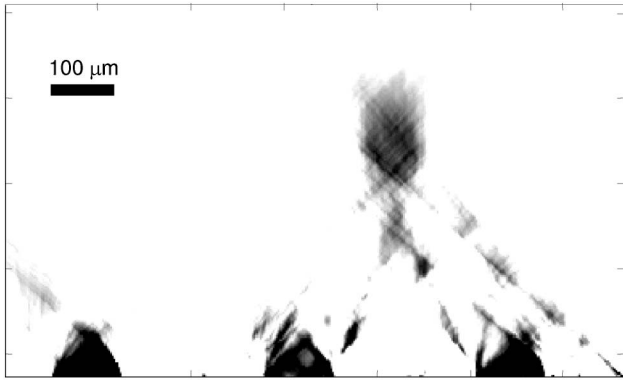


Fig. 11. Inverse Radon transform of slant-stack data.

partly filled in the k space (see Appendix A), leading to artifacts associated with limited-angle tomography. Moreover, within the sample the resolution would be scaled by the inverse of the index, as the range of angles is reduced. Also, in the presence of occlusion, as in the experiment we have conducted, the actual range of rays collected is obviously reduced further, as some rays may be blocked. This would also manifest as a shadow artifact extending axially from the occlusion, covering the region of the image from which no rays can be collected by the objective. If the occlusion is larger than the width of the converging beam, the shadow will reach the object, covering the completely occluded region.

As noted in Section 1, conventional computed tomography involves the collection of some angular range of projections, with a fixed field of view determined by the size of the detector, while here we have a fixed angular range determined by the objective, and we collect data over the field of view serially. As a result, while our angular range is limited by the hardware, the field of view imaged is essentially unlimited in the transverse direction. This trade-off could be useful in applications where rotating or circumnavigating the desired region of the sample is not possible, for example, in imaging near the surface of the skin.

The technique could also be applicable to imaging biological samples, which contain mostly small index variations in addition to highly attenuating regions (e.g., mitochondria and nuclei). It also should be noted that the method can be easily integrated with standard laser scanning confocal microscopy systems. Also, the method could be adapted to other system geometries, such as transmissive or reflective, by adapting the reconstruction algorithm using knowledge of the ray paths.

Appendix A: Three-Dimensional Sheared Radon Transform

Here we extend the idea to three dimensions and review the k -space description of the Radon transform data. First we note how the rearrangement of rays from Fig. 4 to Fig. 5(b) can be directly extended to three dimensions. The detector pixels and focal plane locations fall on planes parallel to the

$y - x$ plane, as in Fig. 12, and the collection of slant-stack data now forms a three-dimensional cube of data.

The collection of data corresponding to a given detector pixel now describes a projection at some angle in both x and y , corresponding to the pixel's relationship to the focal point. In three dimensions, we have shears both in x and y . So the coordinate transform for both shears would be

$$(x, y, z) \rightarrow (x - z \tan \theta_{xz}, y - z \tan \theta_{yz}, z), \quad (\text{A1})$$

which we can write in matrix form as

$$\mathbf{x}' = \mathbf{A}\mathbf{x}, \quad (\text{A2})$$

where $\mathbf{x} = (x, y, z)^T$, as usual [we will also interchangeably use notation such as $f(\mathbf{x}) = f(x, y, z)$ when convenient], and we similarly will use $\mathbf{k} = (k_x, k_y, k_z)^T$ for the frequency domain. The shearing matrix is

$$\mathbf{A}_{\theta_{xz}, \theta_{zx}; \theta_{yz}, \theta_{zy}} = \begin{pmatrix} 1 & 0 & -\tan \theta_{zx} \\ 0 & 1 & -\tan \theta_{zy} \\ -\tan \theta_{xz} & -\tan \theta_{yz} & 1 \end{pmatrix}, \quad (\text{A3})$$

where the x and y coordinates are only sheared with respect to z , or vice versa. In the case of Eq. (A2) we have $\mathbf{A}_{0, \theta_{zx}, 0; -\theta_{zy}, 0}$. Then the shearing of the k space that results from the shearing of the coordinate system is

$$\begin{aligned} F(\mathbf{k}) &= FT\{f(\mathbf{x})\}, \\ F(\mathbf{A}_{-\theta_{zx}, 0; -\theta_{zy}, 0}\mathbf{k}) &= FT\{f(\mathbf{A}_{0, \theta_{zx}, 0; 0, \theta_{zy}}\mathbf{x})\}. \end{aligned} \quad (\text{A4})$$

So when the x and y coordinates are sheared with respect to z , the Fourier transform has its z coordinate sheared with respect to x and y by the negative of the shearing angles.

Now we reconsider the projection-slice theorem with shearing transformations. From the usual zero-angle starting point:

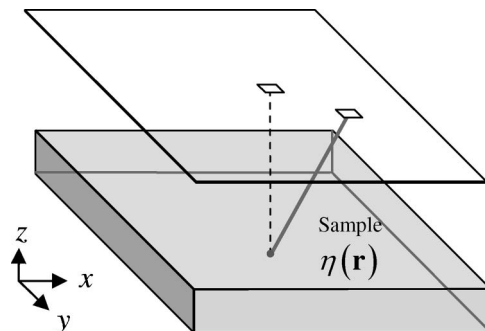


Fig. 12. Ray between focal point and detector pixel in 3D.

$$\begin{aligned}
p_0(x,y) &= \int f(x,y,z)dz, \\
P_0(k_x,k_y) &= \iint p_0(x,y)e^{-j[xk_x+yk_y]}dxdy, \\
&= F(k_x,k_y,0).
\end{aligned} \tag{A5}$$

So the unsheared projection is the horizontal slice of the Fourier transform. The projection through a sheared version of the data will be the horizontal slice of the sheared data's Fourier transform, which is itself a sheared version of the original Fourier transform from Eq. (A4).

Consider sheared data:

$$\begin{aligned}
g(\mathbf{x}) &= f(\mathbf{A}_{0,\theta_{zx},0,\theta_{zy}}\mathbf{x}), \\
&= f(x-z\tan\theta_{zx},y-z\tan\theta_{zy},z), \\
G(\mathbf{k}) &= F(\mathbf{A}_{-\theta_{zx},0,-\theta_{zy},0}\mathbf{k}), \\
&= F(k_x,k_y,k_z+k_x\tan\theta_{zx}+k_y\tan\theta_{zy}).
\end{aligned} \tag{A6}$$

The projection of these data,

$$\begin{aligned}
p_\theta(x,y) &= \int g(x,y,z)dz, \\
P_\theta(k_x,k_y) &= G(k_x,k_y,0), \\
&= F(k_x,k_y,0+k_x\tan\theta_{zx}+k_y\tan\theta_{zy}),
\end{aligned} \tag{A7}$$

is a slice through a sheared plane of the Fourier transform. Also we can see that the k_x and k_y dimensions have not been scaled (as they are in the case of rotation). Hence, the sample spacing in those dimensions remains unchanged with shearing. So interpolation in k_x and k_y is not needed.

Now we consider sampled k -space data. If the projection is sampled with spacing as Δ in x and y , then the sampling frequency is Δ^{-1} . An N -point discrete Fourier transform (DFT) of the zeroth projection will produce samples in k space with spacing $(N\Delta)^{-1}$ in both k_x and k_y . The k -space samples will, therefore, be at locations $((N\Delta)^{-1}s, (N\Delta)^{-1}t, 0)$, where s and t are integers. For a sheared projection, the locations of k -space samples for the DFT will fall on spatial frequencies (see Fig. 13):

$$\begin{aligned}
(k_x,k_y,k_z) &= ((N\Delta)^{-1}s, (N\Delta)^{-1}t, (N\Delta)^{-1}s\tan\theta_{zx} \\
&\quad + (N\Delta)^{-1}t\tan\theta_{zy}).
\end{aligned} \tag{A8}$$

The volume corresponding to each pixel in k space is

$$\begin{aligned}
\Delta k_x\Delta k_y\Delta k_z &= [(N\Delta)^{-1}][(N\Delta)^{-1}][(N\Delta)^{-1}s\tan\theta \\
&\quad + (N\Delta)^{-1}t\tan\theta], \\
&= (N\Delta x)^{-3}\tan\Delta\theta(s+t),
\end{aligned} \tag{A9}$$

where $\Delta\theta$ is the angular spacing of the projections, which we have assumed is constant:

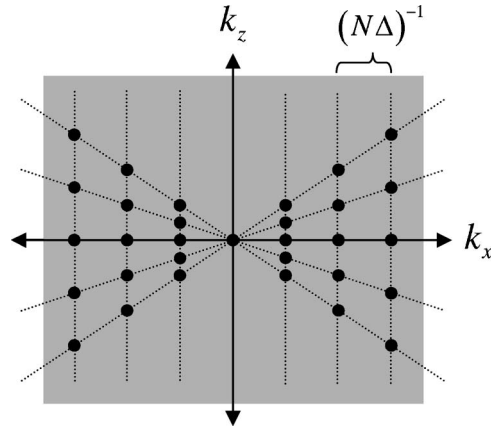


Fig. 13. Locations of discrete samples in k space on the $k_x - k_z$ plane.

$$\begin{aligned}
\Delta k_x\Delta k_y\Delta k_z &= [(N\Delta)^{-1}][(N\Delta)^{-1}][(N\Delta)^{-1}s\tan\Delta\theta(m_x) \\
&\quad + (N\Delta)^{-1}t\tan\Delta\theta(m_y)],
\end{aligned} \tag{A10}$$

where $\Delta\theta(m_x)$ and $\Delta\theta(m_y)$ are the angle spacing between successive detector pixels and the focus at pixel numbers m_x and m_y . If we assume these are the constant $\Delta\theta$, we get

$$\Delta k_x\Delta k_y\Delta k_z = (N\Delta x)^{-3}\tan\Delta\theta(s+t). \tag{A11}$$

The density of pixels is, therefore, the inverse of this, and the amplitude of the filter needed to normalize the pixel density in a backprojection algorithm would be the inverse again of the pixel density. So the appropriate backprojection filter is a linear high-pass filter similar to the rotational case:

$$H(k) \propto |k_x + k_y|. \tag{A12}$$

However, with very large numerical apertures, the change in angle between successive detector pixels becomes significantly smaller at large angles, and a filter that more accurately fits Eq. (A10) must be used.

We are thankful to Fabio Bonomelli and Lin Pang for helping in the assembly and operation of the experiments performed in this research. We gratefully acknowledge support from the National Science Foundation (NSF) and the Defense Advanced Research Projects Agency (DARPA).

References

1. S. W. Paddock, "Principles and practices of laser scanning confocal microscopy," *Mol. Biotechnol.* **16**, 127–149 (2000).
2. S. R. Deans, *The Radon Transform and Some of Its Applications* (Wiley, 1983).
3. T. M. Buzug, *Computed Tomography: From Photon Statistics to Modern Cone-Beam CT* (Springer, 2008).
4. J. Devaney, "Reconstructive tomography with diffracting wavefields," *Inverse Probl.* **2**, 161–183 (1986).

5. D. A. Boas, D. H. Brooks, E. L. Miller, C. A. DiMarzio, M. Kilmer, R. J. Gaudette, and Q. Zhang, "Imaging the body with diffuse optical tomography," *IEEE Signal Process. Mag.* **18**, 57–75 (2001).
6. J. Beuthan, O. Minet, J. Helfmann, M. Herrig, and G. Muller, "The spatial variation of the refractive index in biological cells," *Phys. Med. Biol.* **41**, 369–382 (1996).
7. P. Hariharan, *Optical Interferometry*, 2nd ed. (Elsevier, 2003).
8. T. C. Wedberg, J. J. Stamnes, and W. Singer, "Comparison of the filtered backpropagation and the filtered backprojection algorithms for quantitative tomography," *Appl. Opt.* **34**, 6575–6581 (1995).
9. S. Kawata, O. Nakamura, T. Noda, H. Ooki, K. Ogino, Y. Kuroiwa, and S. Minami, "Laser computed-tomography microscope," *Appl. Opt.* **29**, 3805–3809 (1990).
10. A. M. Zysk, J. J. Reynolds, D. L. Marks, P. S. Carney, and S. A. Boppart, "Projected index computed tomography," *Opt. Lett.* **28**, 701–703 (2003).
11. O. Renaud, J. Viña, Y. Yu, C. Machu, A. Trouvé, H. Van der Voort, B. Chalmond, and S. L. Shorte, "High-resolution 3-D imaging of living cells in suspension using confocal axial tomography," *Biotechnol. J.* **3**, 53–62 (2008).
12. J. Sharpe, U. Ahlgren, P. Perry, B. Hill, A. Ross, J. Hecksher-Sorensen, R. Baldock, and D. Davidson, "Optical projection tomography as a tool for 3D microscopy and gene expression studies," *Science* **296**, 541–545 (2002).
13. S. Kikuchi, K. Sonobe, and N. Ohyama, "Three-dimensional microscopic computed tomography based on generalized Radon transform for optical imaging systems," *Opt. Commun.* **123**, 725–733 (1996).
14. G. N. Vishnyakov, G. G. Levin, V. L. Minaev, V. V. Pickalov, and A. V. Likhachev, "Tomographic interference microscopy of living cells," *Microscopy Anal.* **18**, 15–17 (2004).
15. N. Lue, W. Choi, G. Popescu, K. Badizadegan, R. R. Dasari, and M. S. Feld, "Synthetic aperture tomographic phase microscopy for 3D imaging of live cells in translational motion," *Opt. Express* **16**, 16240–16246 (2008).
16. D. L. Marks, S. C. Schlachter, A. M. Zysk, and S. A. Boppart, "Group refractive index reconstruction with broadband interferometric confocal microscopy," *J. Opt. Soc. Am. A* **25**, 1156–1164 (2008).